Journal of Catalysis **207,** 113–126 (2002)
doi:10.1006/jcat.2002.3511, available online at http://www.idealibrary.com on IDEAL®

Physicochemical Characterization of Isomorphously Substituted FeZSM-5 during Activation

J. Pérez-Ramírez,*,[1] G. Mul,* F. Kapteijn,* J. A. Moulijn,* A. R. Overweg,† A. Doménech,‡ A. Ribera,§ and I. W. C. E. Arends§

*Industrial Catalysis, DelftChemTech, Delft University of Technology, Julianalaan 136, 2628 BL, Delft, The Netherlands; †Interfacultair Reactor Instituut, Delft University of Technology, Mekelweg 15, 2629 JB Delft, The Netherlands; ‡Department of Analytical Chemistry, University of Valencia, Dr. Moliner 50, 46100, Burjassot, Valencia, Spain; and §Laboratory for Organic Chemistry and Catalysis, Julianalaan 136, 2628 BL, Delft, The Netherlands

Received October 17, 2001; revised December 19, 2001; accepted December 19, 2001

Physicochemical characteristics of isomorphously substituted FeZSM-5 both after preparation and after activation have been determined by gas (Ar and N_2) physisorption, ^{27}Al and ^{29}Si magic-angle spinning–nuclear magnetic resonance, NH_3 temperature-programmed desorption, transmission electron microscopy, H_2 temperature-programmed reduction (TPR), ^{57}Fe Mössbauer spectroscopy, and voltammetric response techniques. The activation of as-synthesized FeZSM-5 comprises calcination at 823 K and a subsequent steam treatment (300 mbar of H_2O in N_2) at 873 K. Calcination leads to complete removal of the template. During this process a significant fraction of iron is dislodged to extraframework positions (ca. 50%), while Al is hardly affected. Steam treatment leads to significant dealumination of the zeolite structure, the complete extraction of isomorphously substituted iron, and the clustering of extraframework iron species into highly dispersed oxide nanoparticles of 1–2 nm, containing Fe and probably Al. Various Fe species were identified in the final catalyst. A large fraction of iron in the steamed FeZSM-5 catalyst is in the form of these iron oxide nanoparticles. No larger particles were identified. Apart from these nanoparticles, framework iron, extraframework isolated iron ions, and small oligonuclear oxo-iron complexes in the zeolite channels were identified by Mössbauer spectroscopy and voltammetry. Steam treatment of FeZSM-5 decreases the density and strength of acid sites and leads to mesopore formation (around 11 nm), while the apparent crystalline structure and morphology are not altered. In the steamed sample, at room temperature, iron is mainly present as Fe(III), with a fraction of Fe(II) (at least 10%). H_2-TPR indicates that the fraction of Fe(II) in the material increases up to 50% by pretreatment in He at 623 K, by autoreduction of Fe(III) species. The fraction of Fe(III) reduced to Fe(II) depends on the duration of this pretreatment and appears to involve different species in the catalyst. © 2002 Elsevier Science (USA)

Key Words: **FeZSM-5; isomorphous substitution; activation; steam treatment; characterization; iron species; nanoparticles; Mössbauer; electrochemistry.**

INTRODUCTION

Fe-based zeolites with MFI structure, including ZSM-5 and silicalite, are receiving increasing attention in the literature. Reactions catalyzed by these materials include isomerization and oxidative dehydrogenation of alkanes (1, 2), and selective oxidation of benzene to phenol using N_2O as the oxidant (3, 4). FeMFI also plays an important role in environmental catalysis for the reduction of NO_x and N_2O with hydrocarbons (HC-SCR) or ammonia (NH_3-SCR) (5–12), direct N_2O decomposition (13, 14), and selective oxidation of NH_3 to N_2 with O_2 (15).

Various techniques have been described in the literature to characterize Fe-zeolites, including transmission electron microscopy (TEM), Fourier transform infrared, temperature-programmed reduction (TPR), electron spin resonance, and recently extended X-ray absorption fine structure (14, 16–23). Different forms of iron have been identified in FeZSM-5 (Fig. 1). These include isolated ions either (a) in framework positions (isomorphously substituted) or (b) in cationic positions in the zeolite channels, (c) binuclear and, in general, oligonuclear iron complexes in extraframework positions, (d) iron oxide FeO_x nanoparticles of size $\leq$2 nm, and (e) large iron oxide particles (Fe_2O_3) in a wide distribution (up to 25 nm in size) located at the surface of the zeolite crystal.

FeZSM-5 catalysts are often prepared by solid- and liquid-ion exchange, or sublimation methods, using commercial zeolites. Calcination of these materials usually leads to the formation of a significant fraction of large iron oxide particles (see Fig. 1e), which are known to be inactive in the different reactions catalyzed by FeZSM-5 (3, 6, 9, 17). Also, ion-exchange methods often lack reproducibility (16, 24), which makes them unattractive from a catalytic point of view. Chemical vapor deposition (CVD) of $FeCl_3$ in the channels of H–ZSM-5 is undoubtedly a superior method for preparing FeZSM-5. The water-free conditions under which the exchange takes place allow full exchange of the

[1] To whom correspondence should be addressed. Fax: +31 15 278 5006. E-mail: j.perezramirez@tnw.tudelft.nl.

0021-9517/02 $35.00

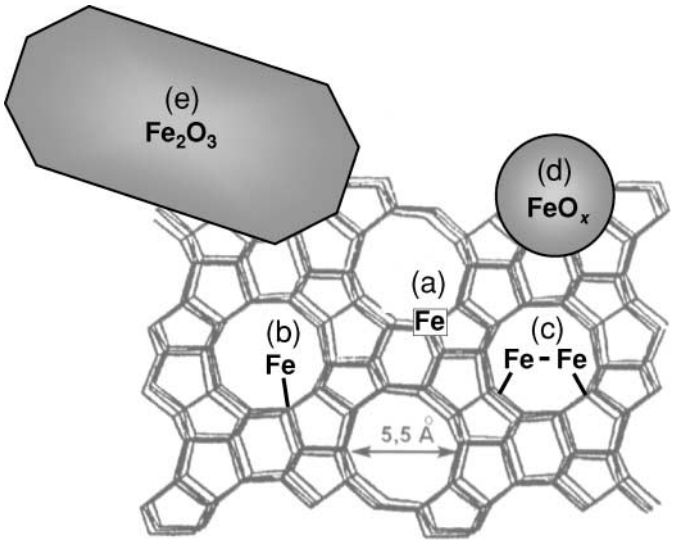

FIG. 1. Schematic representation of the different Fe species identified in FeZSM-5.

ZSM-5 zeolite, where iron is mainly present in the form of binuclear hydroxide clusters at ion-exchange positions. However, in this case, the treatments after the CVD exchange strongly affect the state of the iron species. Calcination of the exchanged sample before a hydrolysis step mainly leads to the formation of large iron oxide (hematite) particles (18). The heating rate during calcination was also found crucial in the development of these particles (25, 26).

In an earlier paper (20), some of us reported the performance of steamed FeZSM-5 for selective oxidation of benzene to phenol with N_2O, displaying high phenol productivities (0.8 mmol of phenol $\cdot h^{-1} \cdot g^{-1}$ during 7 h time on stream). This catalyst, hereafter denoted *ex*-FeZSM-5, was prepared by the hydrothermal synthesis of isomorphously substituted FeZSM-5, followed by calcination at 823 K and steam treatment at 873 K. We recently reported that *ex*-FeZSM-5 also yields significantly higher N_2O decomposition activity (on a per Fe basis) than catalysts prepared via other procedures, such as liquid (aqueous)- or solid-ion exchange and sublimation (26, 27). Furthermore, an improved stability for direct N_2O decomposition in the presence of O_2, NO, SO_2, and H_2O, typically present in tail-gases from nitric acid manufacture and combustion processes, has been observed (26, 27).

The nature of the active Fe species of *ex*-FeZSM-5 in the N_2O-mediated benzene to phenol was previously investigated by some of us using ultraviolet–visible (UV–vis), X-ray diffraction (XRD), and electron paramagnetic resonance (EPR) (20). UV–vis analysis showed that steam treatment induces the migration of Fe to extraframework positions, without an apparent modification of the long-range ordering of the crystalline structure, as concluded from XRD. From EPR, two redox active species were identified but an unambiguous assignment of the iron species in the catalyst could not be given. Although different authors have investigated the extraction of iron from isomorphously substituted Fe-silicalite upon thermal treatment in the range of 773–1073 K in air (28, 29), a detailed characterization of the activation of the FeZSM-5 and nature of the species formed by the steaming procedure has not been reported.

In this paper, a detailed characterization of the activation of isomorphously substituted FeZSM-5 by calcination and steaming is presented, based on gas (Ar, N_2) physisorption, ^{27}Al and ^{29}Si magic-angle spinning (MAS)–nuclear magnetic resonance (NMR), TEM, NH_3 temperature-programmed desorption (TPD), H_2-TPR, ^{57}Fe Mössbauer spectroscopy, and voltammetric response techniques. The results lead to a detailed description of the physicochemical changes induced by the postsynthesis treatments, as well as of the nature of the different species in the catalysts.

EXPERIMENTAL

Material Preparation

The isomorphously substituted FeZSM-5 was synthesized hydrothermally using tetrapropylammonium hydroxide as the template (20). A solution of the silica source (tetraethylorthosilicate, TEOS, Acros, 98%), the template (tetrapropylammonium hydroxide, TPAOH, Fluka, 20% in water), and NaOH was added to a mixture of aluminum(III) nitrate ($Al(NO_3)_3 \cdot 9H_2O$, Merck, 99%) and iron(III) nitrate ($Fe(NO_3)_3 \cdot 9H_2O$, Merck, 98.5%). The molar ratios between components were $H_2O/Si = 45$, $TPAOH/Si = 0.1$, $NaOH/Si = 0.2$, $Si/Al = 36$, and $Si/Fe = 152$. The solution was transferred to a stainless-steel autoclave lined with Teflon and kept in a static air oven at 448 K for 5 days. The crystalline material was filtered and washed with deionized water until the sample was free of nitrates. The as-synthesized sample (FeZSM-5*as*), in which Fe(III) is isomorphously substituted in the zeolite framework, was calcined in air at 823 K for 10 h and was then converted into the H-form by three consecutive exchanges with an ammonium nitrate solution (0.1 M) overnight and subsequent calcination at 823 K for 5 h (FeZSM-5*c*). Finally, the catalyst was steamed at ambient pressure (water partial pressure of 300 mbar and 30 ml $\cdot$ min^{-1} of N_2 flow) at 873 K during 5 h, yielding *ex*-FeZSM-5. The sample was stored at room temperature in dry atmosphere.

In order to perform ^{57}Fe Mössbauer measurements with the different samples, ^{57}Fe-enriched FeZSM-5*as* was prepared. For this purpose, a small piece of ^{57}Fe foil was dissolved in concentrated nitric acid (1 M). Subsequently, ammonium hydroxide was added to neutralize the solution, followed by addition of the aluminum source. The synthesis and postsynthesis treatments were as described above.

Characterization

The chemical composition of the catalysts was determined by inductively coupled plasma optical emission spectroscopy (Perkin–Elmer Plasma 40 (Si) and Optima 3000DV (axial)) and atomic absorption spectroscopy (Perkin-Elmer 1100).

Ar adsorption isotherms at 87 K were obtained in a Micromeritics ASAP 2010 apparatus. The pore size distribution was calculated from the adsorption branch of the isotherm using the Saito–Foley model (30). N_2 adsorption at 77 K was carried out in a QuantaChrome Autosorb-6B apparatus. The pore size distribution was calculated from the desorption branch of the isotherm using the Barret–Joyner–Halenda model (31). Samples were previously evacuated at 623 K for 16 h. The BET method was used to calculate the surface area (S_{BET}) of the samples, while the micropore volume (V_{micro}) and external surface area (ESA) were determined using the *t*-plot method according to Lippens and de Boer (32).

^{29}Si and ^{27}Al MAS–NMR were recorded at 79.46 and 104.26 MHz, respectively, with a Varian VXR-400S spectrometer. The narrow-bore magnet (50 nm) was fitted with a high-speed magic spinning (MAS) Doty probe. The samples were spun in 5-mm-diameter rotors made of zirconia. The length of the radio frequency pulses was 3.1 μs for Si and 0.5 μs for Al. The spinning frequency was in the range 4–4.5 kHz for Si and 7.0 kHz for Al. Acquisition time was 0.05 s for Si and 0.2 s for Al. A time interval of 5 s for Si and 1 s for Al between successive accumulations was selected in order to avoid saturation effects. The number of accumulations (688 for Si and 10,000 for Al) allowed a signal-to-noise ratio higher than 20. The ^{27}Al and ^{29}Si chemical shifts were referenced to $Al(H_2O)_6^{3+}$ and $Si(CH_3)_4$, respectively.

Temperature-programmed desorption of ammonia (NH_3-TPD) measurements were carried out on a Micromeritics TPR/TPD 2900 equipped with a thermal conductivity detector (TCD). The sample (40 mg) was pretreated at 723 K in He (50 ml $\cdot$ min^{-1}) for 1 h. Afterward, NH_3 (40 ml $\cdot$ min^{-1}) was adsorbed at 473 K. After 15 min of adsorbing NH_3 a flow of He (50 ml $\cdot$ min^{-1}) was passed through the reactor over the course of 30 min to remove weakly adsorbed NH_3 on the catalyst surface. This procedure was repeated three times. Desorption of NH_3 was monitored in the range of 473–873 K at 10 K $\cdot$ min^{-1}.

Transmission electron microscopy (TEM) was carried out on a Philips CM 30 T electron microscope with a LaB_6 filament as the source of electrons operated at 300 kV. Samples were mounted on a copper-supported carbon polymer grid by placing a few droplets of a suspension of ground sample in ethanol on the grid, followed by drying at ambient conditions. In order to enhance the visibility of the small particles, the zeolites were amorphized by the electron beam. This process did not induce sintering of iron oxide particles in the specimen.

Temperature-programmed reduction (H_2-TPR) was performed in a home-made fixed-bed reactor (4-mm inner diameter) setup, using a high-purity mixture of 7.7 vol% H_2 in Ar to reduce samples in the temperature range of 298–1273 K. Copper(II) oxide was used for calibration. The sample mass was diluted with SiC (volumetric ratio 1 : 1) in order to improve heat transfer in the catalyst bed. The following procedure was applied: (i) heating in He (or 10 vol% N_2O in He) at 623 K for 2 or 15 h, (ii) cooling to room temperature in the same gas, (iii) flushing with He over the course of 1 h at room temperature (in the case of N_2O pretreatment), and (iv) switching to the reductive H_2 in the Ar mixture and starting the temperature program (heating rate, 10 K $\cdot$ min^{-1}). A fresh sample was used for each H_2-TPR experiment. The gas at the reactor exit was passed through a membrane drier to remove vapors and condensable gases before entering the TCD.

^{57}Fe Mössbauer spectra were measured on a constant acceleration spectrometer in a triangular mode with a ^{57}Co : Rh source. Spectra for the different FeZSM-5 samples were obtained at 300, 77, and 4.2 K. The overall spectra were deconvoluted with calculated Mössbauer spectra that consisted of Lorentzian-shaped lines. In the case of quadrupole doublets the line widths and the absorption areas of the constituent lines were constrained equally. Positional parameters were not constrained in the fitting procedure. Isomer shift values are reported relative to sodium nitroprusside. The accuracy of the positional parameters is ± 0.03 mm $\cdot$ s^{-1}.

The voltammetric response of graphite–polyester composite electrodes (GPCEs) modified by FeZSM-5 samples was measured in a standard three-electrode arrangement with a platinum auxiliary electrode and a saturated calomel reference electrode (SCE). Preparation of the composite electrode and modification by FeZSM-5 have been described elsewhere (33). Linear scan voltammograms (LSVs) and differential pulse voltammograms (DPVs) were recorded at a potential scan rate (ν) of 20 mV $\cdot$ s^{-1} and pulse amplitude (ΔU) of 80 mV using a Metrohm E506 Polarecord. Experiments were performed at 298 K in aqueous solutions of 0.1–1.0 M HCl (supporting electrolyte) under argon atmosphere. Hematite (Fe_2O_3, Fluka, 98%), goethite (FeO(OH), Fluka, 98%), and $FeCl_3 \cdot 6H_2O$ (Aldrich, >99%) were used as reference materials.

RESULTS AND DISCUSSION

Chemical Composition

The elemental analysis of the as-synthesized, calcined, and steamed FeZSM-5 samples prepared in this study is summarized in Table 1. Comparison of the composition of the gels and the crystalline samples suggests that all the iron and aluminum is present in the solid, while a small part of the silicon is not incorporated. Only minor differences

TABLE 1

Chemical Composition and Other Characterization Data of the Crystalline Samples Used in this Study

Sample	FeZSM-5*as*[a]	FeZSM-5*c*	*ex*-FeZSM-5
Si/Al	31.1	31.6	31.3
Si/Fe	126.2	124.9	121.7
Na (wt%)	0.44	<0.01[d]	<0.01
Fe (wt%)	0.59	0.64	0.67
S_{BET}[b] ($m^2 \cdot g^{-1}$)	—	425	395
ESA[c] ($m^2 \cdot g^{-1}$)	—	23	33
V_{total} ($cm^3 \cdot g^{-1}$)	—	0.24	0.23
V_{micro}[c] ($cm^3 \cdot g^{-1}$)	—	0.16	0.14

[a] Metal molar ratio in the synthesis gel: Si/Al = 36 and Si/Fe = 152.
[b] BET method.
[c] *t*-plot method.
[d] Detection limit of ICP-OES.

between the as-synthesized sample and the posttreated samples can be observed. The concentration of Na in the calcined and steamed FeZSM-5 is below detection limits.

The color changes caused by the postsynthesis treatments (especially steaming) can be nicely followed by the naked eye. The as-synthesized and calcined samples were white (the last sample had a slight tinge). The accumulation of iron oxide/hydroxide in the zeolitic voids on steaming changed the nearly white color to light brownish.

Gas (Ar and N_2) Physisorption

Ar adsorption at 87 K was carried out to investigate changes in the microporosity of FeZSM-5 before and after steam treatment. The micropore size distribution of FeZSM-5*c* shows a well-defined peak at 0.56 nm ($p/p_0 = 10^{-5}$) (Fig. 2a), characteristic of the channels in the MFI structure. By steaming, a bimodal distribution is apparently obtained (at 0.56 and 0.8 nm). The intensity of the peak at 0.56 nm diminishes in *ex*-FeZSM-5 compared to FeZSM-5*c*, and the peak at 0.8 nm develops. This suggests disappearance of micropores, which is confirmed by the cumulative curve. This is in agreement with the slightly lower specific surface area S_{BET} of the steamed sample (Table 1). Llewellyn *et al.* (34) explained by isothermal volumetry, microcalorimetry, and neutron diffraction techniques on silicalite-1 that the relatively sharp peak centered at 0.8 nm ($p/p_0 = 10^{-3}$) is an artifact, caused by the transition of Ar molecules from a *disordered phase* (presumably a fluid) to a *crystalline-like solid phase* at the corresponding relative pressure. The appearance of this transition depends on the Si/Al ratio in the sample (35). It is proposed that a high-framework Si/Al ratio (Si/Al > 23) leads to a more homogeneous energetic state of the zeolite surface toward Ar adsorption (34, 35). The presence of the artifact is therefore an indication that dealumination of the zeolite framework has occurred.

The mesopore size distribution derived from the desorption branch of the N_2 isotherm of FeZSM-5*c* and *ex*-FeZSM-5 (Fig. 2b) shows different contributions. A broad peak centered at around 11 nm is identified in *ex*-FeZSM-5, which suggests the formation of mesopores, leading to a significant increase in the ESA (Table 1) by creation of intercrystalline voids. Scanning electron micrographs of the as-synthesized, calcined, and steamed FeZSM-5 samples showed no change in crystal morphology during the postsynthesis treatments (20). As a consequence of mesopore formation, the micropore volume and the total pore volume in the steamed sample are slightly lower than in the calcined sample. This should be related to the presence of the generated extraframework species (mainly Al) in the

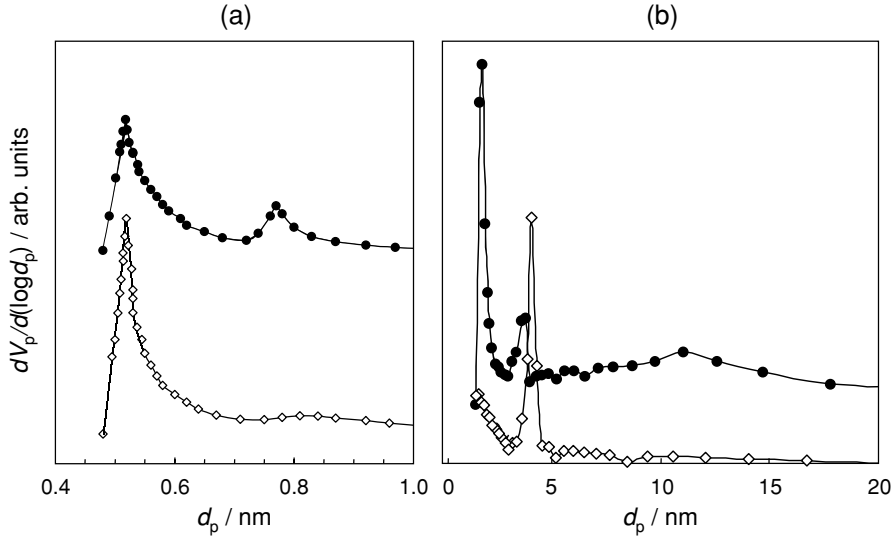

FIG. 2. Pore size distribution of (◇) FeZSM-5*c* and (●) *ex*-FeZSM-5, calculated from (a) Ar at 87 K and (b) N_2 adsorption at 77 K isotherms, using Saito–Foley model and Barret–Joyner–Halenda model, respectively.

channels of the zeolite, inducing pore blockage. The mesopores are likely to be formed as a consequence of the extraction of Al and Fe in the steaming procedure from framework positions. This leads to lattice defects, which can be restored with Si atoms coming from external parts of the zeolite crystal (36). As a result, the framework becomes more siliceous and adjacent cages become interconnected through removal of Si from the least stable parts of the lattice. A local character of this process is inferred by XRD results (20) showing no change in the crystal structure of the calcined and steamed samples.

The peak at 3.9 nm ($p/p_0 = 0.45$) is also an artifact, attributed to the tensile strength effect of the liquid N_2 adsorbate at 77 K during desorption (37). The pore size distribution in the range of pore sizes from 2 to 3.9 nm differs in the calcined and steamed materials. The sharp peak at 2 nm in the steamed sample, which is less pronounced in the calcined sample, is considered to be the equivalent artifact observed in the Ar adsorption measurements at 0.8 nm ($p/p_0 = 10^{-3}$) (38).

^{27}Al and ^{29}Si MAS–NMR Spectroscopy

^{27}Al and ^{29}Si MAS–NMR spectroscopy were carried out to investigate changes in the coordination of the atoms in the zeolite framework on calcination and steaming. The ^{27}Al MAS–NMR spectra of FeZSM-5*as* and FeZSM-5*c* (Figs. 3a and 3b) exhibit a sharp resonance at 55 ppm, assigned to tetrahedrally coordinated Al atoms in lattice positions (39). In general, the intensities of the signals in the NMR spectra are lower than is typically observed for ZSM-5 containing only Al and Si, as a direct consequence of the paramagnetism of the Fe ions, whose unpaired electrons generate a local magnetic field that strongly perturbs the resonance of the ^{27}Al nuclei. The peaks at −5 and 105 ppm are spinning side bands due to quadrupole interactions of ^{27}Al nuclei. The intensity of the peak at −5 ppm is larger than the spinning band at 105 ppm, suggesting the presence of another signal caused by small amounts of Al in extraframework positions.

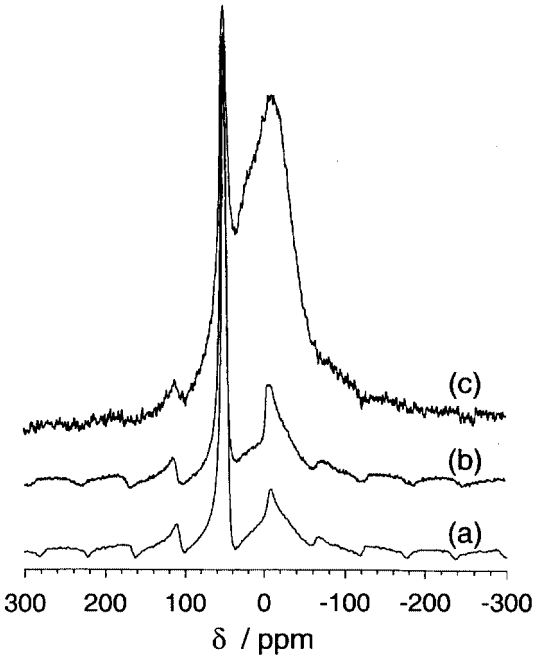

FIG. 3. ^{27}Al MAS–NMR spectra at 300 K of (a) FeZSM-5*as*, (b) FeZSM-5*c*, and (c) *ex*-FeZSM-5.

Calcination of FeZSM-5*as* hardly affects the ^{27}Al MAS–NMR spectrum, in agreement with previous dealumination studies on ZSM-5 zeolites (40). Steam treatment leads to dealumination of the zeolite framework by migration of Al(III) to extraframework positions. In the ^{27}Al MAS–NMR spectrum of *ex*-FeZSM-5 (Fig. 3c), the resonance around 55 ppm significantly decreases and a broad band centered around −3 ppm appears, with a shoulder at approximately 30 ppm. The peak at −3 ppm is attributed to hexacoordinated Al species in octahedral positions (39), while the shoulder at 30 ppm indicates pentacoordinated or highly distorted tetrahedral Al species (41, 42). The broadening of this signal is probably due to the presence of extraframework Al with different coordination and positions in *ex*-FeZSM-5. In view of the spectra acquired, the degree of dealumination is difficult to quantify. From the relative ratio of intensities of the signals at 55 and −3 ppm in the ^{27}Al NMR spectra ($I_{55} + I_{-3}/I_{55}$), it was roughly estimated that ∼30–40% of framework aluminum is dislodged to extraframework positions by the steam treatment. Different extraframework Al species have been considered to be present in zeolite catalysts (36). Which of these species is actually formed on dealumination cannot be assessed from these NMR spectra.

The ^{29}Si MAS–NMR spectra of the as-synthesized and calcined samples (Figs. 4a and 4b) show a broad signal with a maximum at −117 ppm and a shoulder around −120 ppm, corresponding to Si(0Al), and a weak signal at −109 ppm attributed to Si(1Al) (39). The shoulder at −100 ppm, normally attributed to Si(2Al), was not observed in our spectra, indicating a highly dispersed state of Al in the zeolite framework. Dealumination of the calcined sample on steaming is indirectly confirmed by the decrease in the signal at −109 ppm in the ^{29}Si MAS–NMR spectrum (Fig. 4c), indicating the absence of Si nuclei coordinated to aluminum after the dislodgment of Al to extraframework positions.

NH_3-TPD

Steam treatment of FeZSM-5*c* also induces changes in the acidity of the catalyst, as shown by NH_3-TPD (Fig. 5). The two NH_3 desorption peaks identified in FeZSM-5*c* (at 540 and 725 K, Fig. 5a) are indicative of the presence of acidic centers of different strength. According to

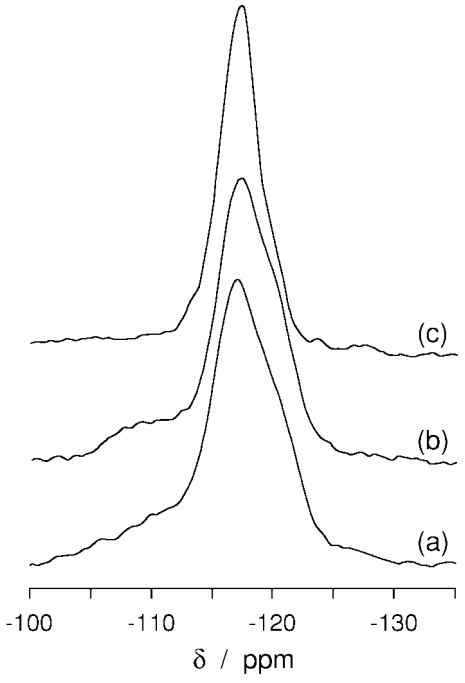

FIG. 4. ^{29}Si MAS–NMR spectra at 300 K of (a) FeZSM-5*as*, (b) FeZSM-5*c*, and (c) *ex*-FeZSM-5.

the literature, the low-temperature peak corresponds to weakly acidic sites and the high-temperature peak (>673 K) to strong sites (22, 43). The strength and number of the acidic sites decrease after the steam treatment, indicating that most of the acidic centers in the calcined sample may be Brønsted acids and arise from the presence of Al and Fe in the framework. The acidic centers in the steamed sample show a broad distribution (at 675 K, Fig. 5b).

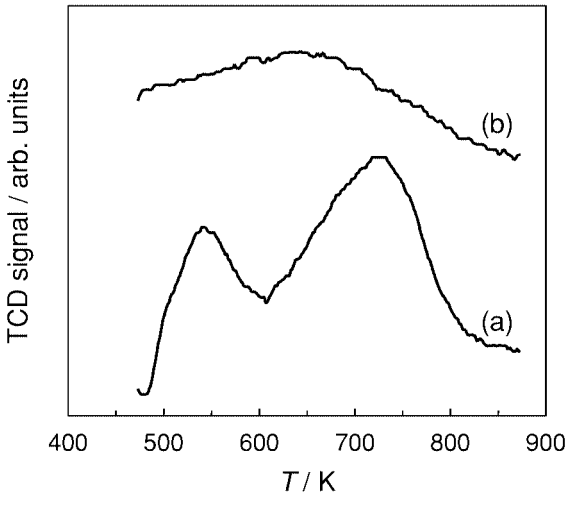

FIG. 5. NH_3-TPD profiles of (a) FeZSM-5*c* and (b) *ex*-FeZSM-5. Heating rate, 10 K · min^{-1}.

TEM Analysis

TEM was used to analyze the extraction of the Fe ions from the zeolite lattice on calcination and steam treatment. The TEM micrograph of FeZSM-5*as* does not show any iron-related phase (Fig. 6a), suggesting that all the Fe(III) is present in a highly dispersed state at isolated positions in the zeolite framework of the as-synthesized material. Calcination of FeZSM-5*as* to yield FeZSM-5*c* extracts some isomorphously substituted Fe to extraframework positions, as concluded from the presence of small iron oxide particles in the TEM micrograph of FeZSM-5*c* (Fig. 6b). Steam treatment massively dislodges iron to extraframework positions, inducing the formation of homogeneously dispersed iron oxide nanoparticles of 1–2 nm (Fig. 6c). The extraframework Al species generated during steam treatment might play a role in the formation of the iron oxide. Marturano *et al.* (24) reported that since Fe and Al oxide compounds have similar structural properties, it can be envisaged that the presence of extraframework Al species might induce the epitaxial growth of the Fe oxides. Following this reasoning, it is likely that the observed particles also contain extraframework Al species. In principle, due to the size of the nanoparticles, they should be present at the external surface of the zeolite crystal. However, the local formation of mesopores of 11 nm identified by N_2 adsorption makes the presence of this species in the porous network of the zeolitic structure feasible.

H_2-TPR

Figure 7 shows the H_2-TPR profiles of the calcined and steamed samples after He and N_2O pretreatment at 623 K. The molar H_2/Fe ratios in these experiments are collected in Table 2. The TPR profile of FeZSM-5*c* pretreated in He (Fig. 7a) shows two maxima, centered at 680 K (with a shoulder at 710 K) and 1000 K. The first peak (including the shoulder) is ascribed to the reduction of extraframework Fe(III) species to Fe(II). The second peak is attributed to a residual fraction of framework Fe(III), which is hard to reduce (28). It is well-known that framework iron is more difficult to reduce than iron in extraframework positions. The temperature difference observed for the two peaks is indicative

TABLE 2

Molar H_2/Fe Consumption Ratios Derived from TPR Experiments after Pretreatment in He or N_2O at 623 K

	Molar H_2/Fe ratio	
Sample	He	N_2O
FeZSM-5*c*	0.38	0.52
ex-FeZSM-5	0.23	0.47

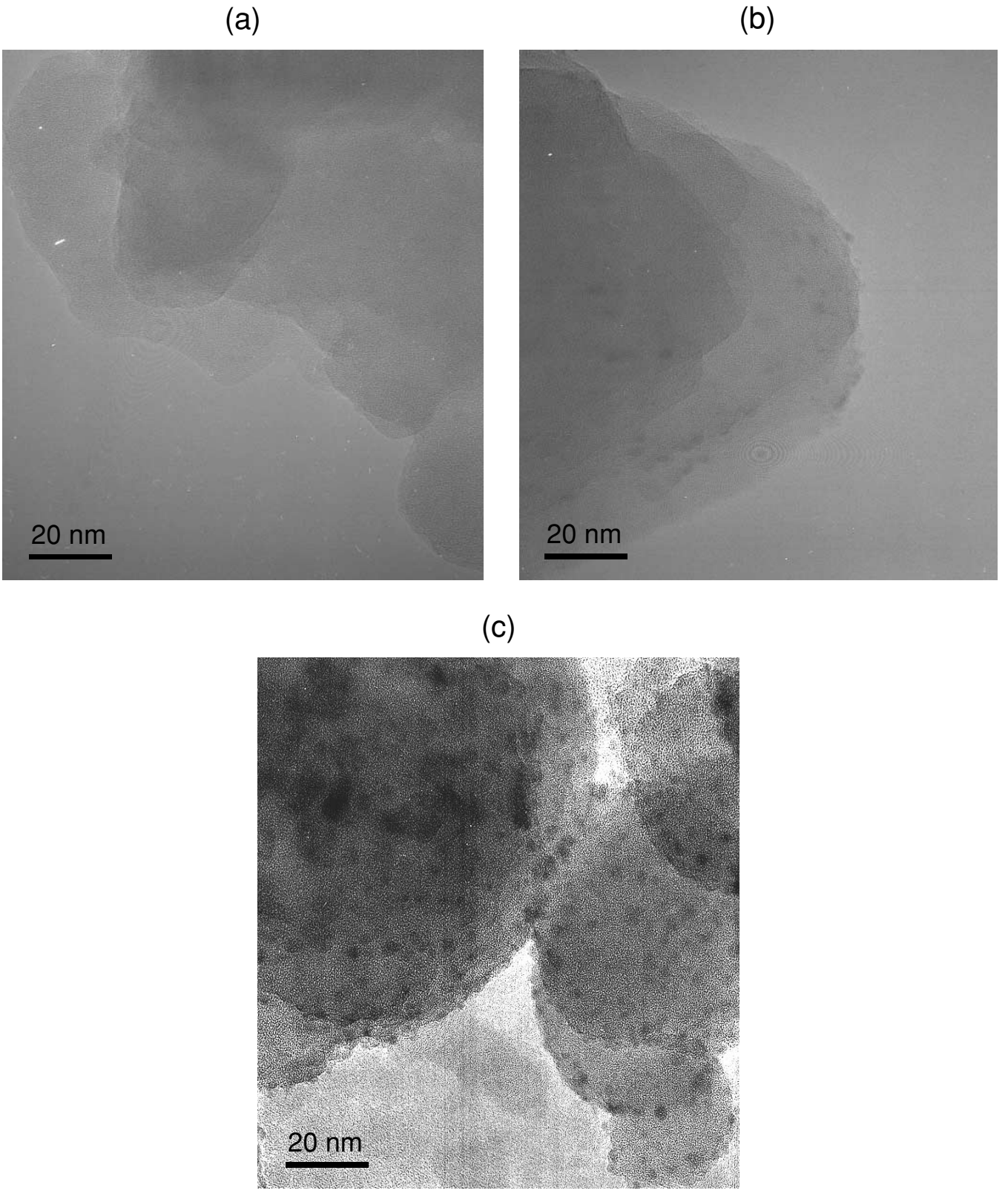

FIG. 6. TEM micrographs of (a) FeZSM-5*as*, (b) FeZSM-5*c*, and (c) *ex*-FeZSM-5.

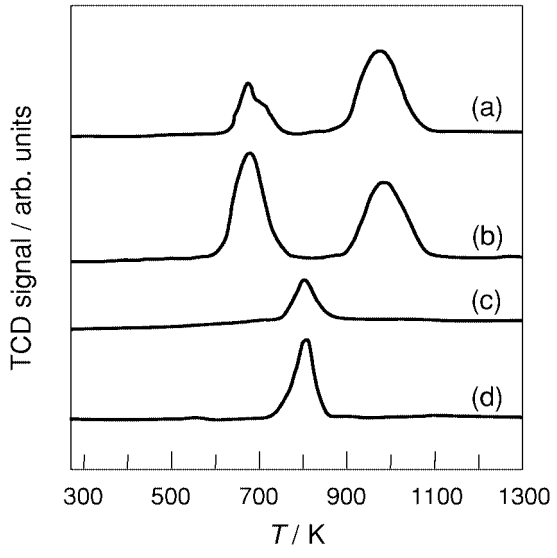

FIG. 7. H_2-TPR profiles of (a) FeZSM-5*c* (He), (b) FeZSM-5*c* (N_2O), (c) *ex*-FeZSM-5 (He), and (d) *ex*-FeZSM-5 (N_2O). Pretreatment of the sample between brackets. Heating rate, 10 K · min^{-1}.

of a great shielding effect of the zeolite framework, which protects framework Fe(III) from reaction with hydrogen. The H_2/Fe ratio in the He-pretreated sample was 0.38. When the sample was pretreated in N_2O at 623 K the H_2/Fe ratio increased to 0.52 (Fig. 7b), which corresponds to the theoretical value (0.5) to reduce all Fe(III) to Fe(II) in the sample:

$$2Fe^{III}O_x + H_2 \rightarrow 2Fe^{II}O_{x-1} + H_2O.$$

Comparing both pretreatments, the area of the first reduction peak increases after the N_2O pretreatment, while the second reduction peak hardly changes compared to the sample pretreated in He. This indicates that a significant amount (~25%) of exclusively the Fe species in extraframework positions is in the Fe(II) oxidation state after calcination at 823 K and pretreatment in He at 623 K.

Lobree *et al.* (44) have shown that the oxidation state and the nature of the iron species in a sublimed FeZSM-5 catalyst depends on the iron content of the zeolite and the pretreatment. Iron was found as Fe(III) in cationic positions as $Fe^{3+}(OH^-)_2$ for molar ratios of Fe/Al < 0.19, whereas above this level the reduction of a fraction of Fe(III) to Fe(II) occurred. Additionally at Fe/Al > 0.56, iron is also present as particles of FeO_x. The formation of Fe(II) is explained by autoreduction of the $Fe^{3+}(OH^-)_2$ species, which are located in highly reducible α sites in ZSM-5 (in the 10-membered ring channel). The autoreduction of FeMFI, i.e., the facile interconversion between Fe(III) and Fe(II) in the zeolite on thermal treatment (>523 K) in inert or vacuum, has been reported by several authors (16, 44–46). The autoreduction process involves release of molecular oxygen and dehydration of initially present $[Fe^{III}(OH)_2]^+Z^-$, leading to $[Fe^{II}(OH)]^+Z^-$, where Z is the zeolite. It is likely that the autoreduction process has also occurred in our calcined sample. From the ratio of the areas of the H_2 consumption peaks (in the N_2O pretreated catalyst) it is estimated that ~50–60% of the framework iron in the as-synthesized material is already extracted by the calcination procedure. This value is higher than previously reported for Fe-silicalite (28), where 20–25% of framework iron was extracted on thermal treatment of the as-synthesized sample in air at 773 K. This difference can be explained by the milder thermal treatment carried out in (28) (773 vs 823 K) and by the fact that isomorphously substituted Fe in silicalite is more stable than in ZSM-5. Analogously, isomorphously substituted Fe in the ZSM-5 framework is less stable than Al (47) and thus substantial extraction of iron takes place on calcination, while all Al remains in framework positions.

In the steamed FeZSM-5 the peak at high temperatures is not present, indicating the absence of framework Fe species in this material. The total H_2/Fe ratio in *ex*-FeZSM-5 pretreated in He at 623 K for 2 h was 0.23 (Fig. 7c), which indicates the presence of ~50% of the iron as Fe(II). Pretreatment of the sample in N_2O leads to a similar pattern (Fig. 7d), with a molar H_2/Fe ratio = 0.47, close to the theoretical value for reduction of Fe(III) to Fe(II). To explain the low H_2/Fe ratio observed in the TPR profiles of *ex*-FeZSM5 after He pretreatment, it can again be assumed that a significant fraction of iron in the sample is already present as Fe(II), suggesting autoreduction in the He pretreatment. The pretreatment of the steamed sample in He for 15 h leads to a lower H_2 consumption (H_2/Fe ~ 0.15), which indicates a clear dependence of the amount of reduced Fe(II) species on the time of the treatment. From the TPR experiments it cannot be assessed accurately whether all Fe(II) in the pretreated samples is caused by autoreduction or if some already exists in the freshly steamed sample (generated on steam treatment). This point will be further addressed by Mössbauer spectroscopy. The reduction peak appears at higher temperatures in *ex*-FeZSM-5 (~815 K) than in FeZSM-5*c* (~680 K), which indicates that the iron species formed after steaming are somehow harder to reduce.

An important feature of the samples investigated in this study is their stability against reduction to Fe^0. This reduction behavior has been observed in highly dispersed Fe-zeolites, containing iron ions at cationic positions (isolated) or small metal complexes (8, 12, 16). Partial or total reduction to metallic iron was observed when preparation routes lead to large iron oxide particles (6, 8, 16). This was not the case in our steamed sample, where the small size of the iron species, including the iron oxide nanoparticles visible in TEM, stabilizes the Fe(II) state on reduction with H_2.

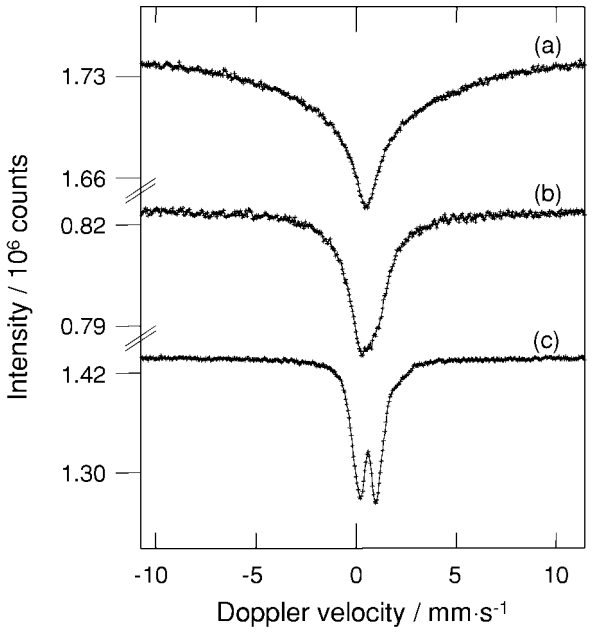

FIG. 8. ^{57}Fe Mössbauer spectra at 300 K in air of (a) FeZSM-5*as*, (b) FeZSM-5*c*, and (c) *ex*-FeZSM-5.

^{57}Fe Mössbauer Spectroscopy

^{57}Fe Mössbauer spectra of as-synthesized, calcined, and steamed FeZSM-5 samples recorded at 300 K in air are shown in Fig. 8. The spectrum of FeZSM-5*as* (Fig. 8a) shows a broad singlet with an average isomer shift, IS = 0.52 mm · s^{-1}, which has been assigned to tetrahedrally coordinated Fe(III) ions (48). Such a broad singlet is typical for paramagnetic iron ions with slow electron spin relaxation, implying large Fe–Fe distances, and thus a homogeneous distribution of Fe(III) ions. This is in perfect agreement with framework incorporation of the iron atoms.

After calcination of the sample a considerable narrowing of the Mössbauer signal is observed together with the onset of a paramagnetic doublet (Fig. 8b). This is the result of shortened electron spin relaxation times, indicating a shortening of the Fe–Fe distances. A likely explanation for these shortened distances is that calcination leads to removal of Fe(III) ions from the ZSM-5 framework. The extraframework species may reside in cationic positions, form small oligonuclear oxo-iron species, and to a minor extent cluster in small nanoparticles, as shown in the TEM micrograph of FeZSM-5*c* (Fig. 6b).

Steam treatment leading to *ex*-FeZSM-5 subsequently gives rise to a well-resolved paramagnetic doublet with an IS = 0.59 mm · s^{-1} and quadrupole splitting of QS = 0.90 mm · s^{-1} (Fig. 8c). The observation of a well-resolved doublet indicates a further increase in electron spin relaxation rates and is interpreted by a continued clustering of Fe(III) ions and small oligonuclear oxo-iron complexes into larger particles. In addition, a small shoulder on the high-energy line of this doublet is fitted with a second doublet with IS = 1.30 mm · s^{-1} and QS = 1.59 mm · s^{-1}. The IS of this doublet suggests that a small part of the iron is present as Fe(II) in the steamed *ex*-FeZSM-5 (10% according to the spectral fitting in Table 3). This Fe(II), which is formed during the steaming procedure, partially explains the relatively low H_2 consumption observed in TPR after He pretreatment at 623 K. The remaining fraction of Fe(II) according to H_2-TPR (40% of the iron in the sample) should be therefore due to autoreduction of Fe(III) to Fe(II) species during He pretreatment in the H_2-TPR experiments.

In order to obtain additional information about the particle size distribution of the iron oxide nanoparticles formed on steam treatment, as well as the oxidation state of the iron atoms in *ex*-FeZSM-5, additional ^{57}Fe Mössbauer spectra were recorded at 300, 77, and 4.2 K applying high vacuum (Fig. 9). Spectral parameters derived from these measurements are presented in Table 3. Two differences can be observed in the ^{57}Fe Mössbauer spectra recorded at 300 K at ambient pressure in air and under high vacuum, respectively (Figs. 8c and 9a): in high vacuum an increased quadrupole splitting of the Fe(II) doublet can be observed, as well as a new broad spectral component with a contribution of 19%. The increased QS = 2.99 mm · s^{-1} of the same Fe(II) species (QS = 1.59 mm · s^{-1} in air and with the same spectral contribution; see Table 3) can be explained by the removal of physisorbed water molecules on evacuation. A justification for this explanation is that reexposure of the evacuated *ex*-FeZSM-5 to ambient air results in a similar Mössbauer spectrum, as presented in Fig. 8c. However, this similarity is observed only after prolonged exposure times

TABLE 3

^{57}Fe Mössbauer Hyperfine Parameters and Relative Intensities of the Fe Species in *ex*-FeZSM-5

Conditions	IS[a] (mm · s^{-1})	QS[b] (mm · s^{-1})	HF[c] (T)	RI[d] (%)	Species
300 K, air	0.59	0.90	—	90	Fe(III)
	1.30	1.59	—	10	Fe(II)
300 K, 1×10^{-6} mbar	0.61	1.02	—	71	Fe(III)
	1.15	—	—	19	—
	1.45	2.99	—	10	Fe(II)
77 K, 1×10^{-6} mbar	0.77	1.14	—	55	Fe(III)
	0.67	—	—	29	
	1.54	3.48	—	13	Fe(II)
	1.62	4.11	—	3	
4.2 K, 1×10^{-6} mbar	0.76	—	48.8	60	Fe(III)
	0.68	1.62	—	22	
	1.65	3.99	—	6	Fe(II)
	1.77	3.08	—	12	

[a] Isomer shift.
[b] Quadrupole splitting.
[c] Average hyperfine field.
[d] Relative intensity.

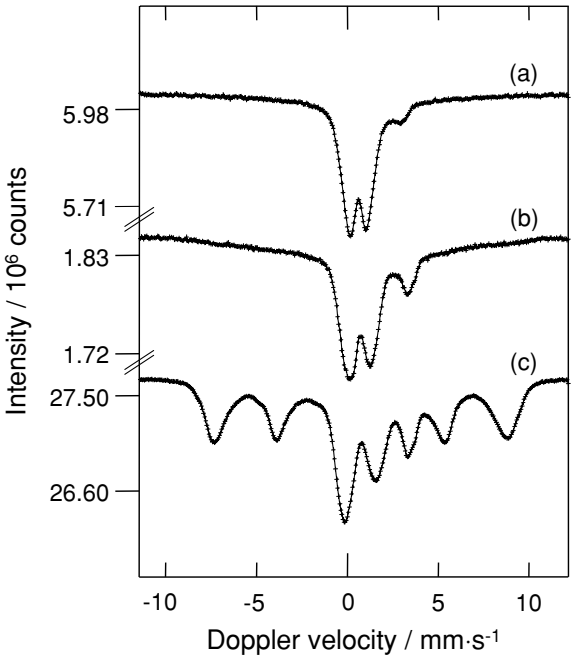

FIG. 9. ^{57}Fe Mössbauer spectra of *ex*-FeZSM-5 measured at (a) 300 K at 1×10^{-6} mbar, (b) 77 K (liquid N_2) at 1×10^{-6} mbar, and (c) 4.2 K (liquid He) at 1×10^{-6} mbar.

(24 h). We explain this slow change as the uptake of water by a slow diffusional process rather than as due to chemical oxidation with molecular oxygen. The latter process should take place at a much faster pace.

The broad singlet with an estimated $IS = 1.15$ mm $\cdot$ s^{-1} can be assigned as follows. Since a fully developed sextuplet is not observed in the spectrum at 77 K (Fig. 9b), it is not conceivable that the observed broad component at 300 K is caused by superparamagnetic iron oxide particles, which are close to the superparamagnetic transition temperature (49). More likely, this spectral component is due to isolated Fe^{3+} ions with slow electron spin relaxation times. Because of the absence of such a component in the spectrum recorded under ambient conditions in air, we believe that these isolated iron atoms reside in extraframework positions. In these positions, the iron atoms are much more affected by the removal of water as a result of the vacuum treatment than when they would be isomorphously substituted. The presence of water in the pores of the zeolite will lead to a mobility of the extraframework iron ions, which makes them invisible for the Mössbauer technique. Water removal by evacuation leads to increased interactions between these cationic iron species and the zeolite framework.

Several observations have been made which favor this argument. First, a strong increase in total resonant absorption area is observed after exposure of the *ex*-FeZSM-5 material to high vacuum. From this, it is deduced that the iron species responsible for this broad component does not absorb resonantly when the material is in contact with air, implying that this iron species is invisible under these conditions. Second, similar to the disappearance of the Fe(II) component, this broad spectral component slowly fades away on reexposure of this evacuated material to air, thereby illustrating the role of water on this reversible process.

The Mössbauer spectrum at 77 K shows the presence of the broad component more prominently, which now also contains the onset of a six-line pattern: a high-spin Fe(III) doublet and two Fe(II) components (Fig. 9b). Although the onset of a six-line pattern clearly indicates slow electron spin relaxation (thus that this component has magnetic character), the assignment of this spectral component is ambiguous. Under the assumption that the broad spectral component observed in the Mössbauer spectrum at 300 K and high vacuum is caused by isolated paramagnetic Fe(III) ions in extraframework positions, it is obvious that this magnetic component is also produced by these iron species. However, since TEM revealed the presence of iron oxide nanoparticles (1–2 nm) this component could be the result of superparamagnetic behavior. This is in agreement with the fact that the spectral contribution of this magnetic component in the Mössbauer spectrum recorded at 77 K has grown partly at the expense of the Fe(III) doublet (see Table 3). At 4.2 K, the magnetic component has developed into a full-grown sextuplet (see Fig. 9c). The spectral contribution of this component has grown to ca. 60% of the total spectral area, again mainly at the expense of the Fe(III) doublet (see Table 3). This is now a clear indication that the iron oxide nanoparticles show superparamagnetic behavior. Broad lines of the sextuplet may suggest an amorphous character of the nanoparticles, with a lower hyperfine field (48.8 T) than in α-Fe_2O_3 (typically 50.2 T). If it is assumed that the broad spectral component in the Mössbauer spectrum recorded at 77 K and with a spectral contribution of 29% is predominantly caused by isolated paramagnetic iron atoms, a particle size close to 2 nm can be estimated for these superparamagnetic iron oxide particles. Additionally, it would mean that the magnetic contribution in the Mössbauer spectrum recorded at 4.2 K is composed of two components, i.e., isolated extraframework iron atoms and iron oxide particles of ca. 2 nm in size, the so-called nanoparticles. It is mentioned in Mössbauer studies by Calis *et al.* (50) on calcined FeZSM-5 samples and, more recently, by Ovanesyan *et al.* (51) on a FeZSM-5 zeolite comparable to that described here that magnetic contributions from isolated paramagnetic iron atoms and superparamagnetic iron oxide particles with slow electron spin relaxation have similar magnetic hyperfine splitting and therefore could largely overlap. Indeed, this result is in excellent agreement with previous research on this catalytic system using EPR spectroscopy. In that case the presence of isolated Fe^{3+} ions in cationic positions was confirmed by the appearance of a

strong band at $g = 6.0$ on calcination and mainly after steam treatment (20). Similar to the observation in the Mössbauer spectrum recorded at 77 K, two Fe(II) components can be discriminated in the spectrum recorded at 4.2 K, although the nature of these Fe(II) sites is at present not clear.

Voltammetric Response

Comparison of electrochemical response of the zeolites during different preparation stages provides valuable information about the disappearance and appearance of distinctive electroactive iron species in the samples. Some of us have recently reported the characterization of steamed FeZSM-5 using Paraloid B72 film electrodes, based on the preparation method of the electrode, the shape of the voltammetric curves, and the dependence of the peak potentials with the pH of the supporting electrolyte and the potential scan rate (52). Although the electron transfer to electroactive species in zeolite is a subject of controversy, we have recently provided evidence that the electrochemical observation corresponds to a "boundary region" of the zeolite (52), situated close to the external surface, in agreement with other authors (53). Therefore, the electrochemistry measured not only corresponds to iron oxide particles at the external surface of the crystal but also to framework iron ions and other small intrazeolitic species strongly attached to the zeolite (i.e., in the channels). However, since the electron transport from the electrode to zeolite (or vice versa) occurs by tunneling, only a fraction of the zeolite crystal is effectively probed. This is ellaborated elsewhere (52).

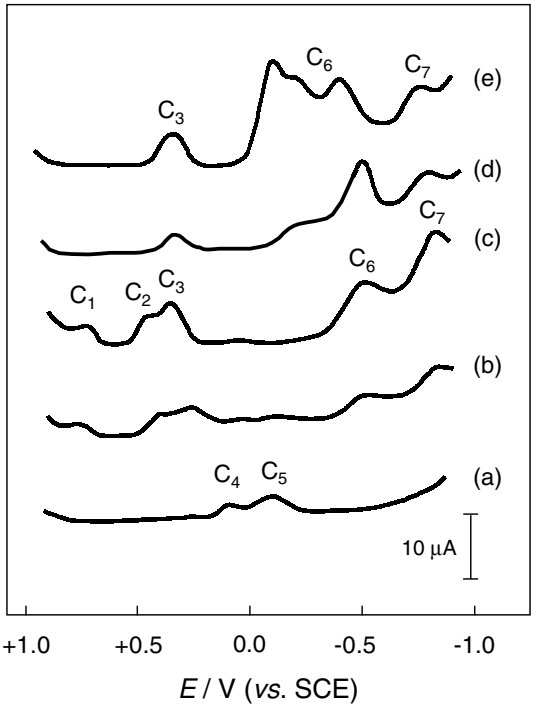

FIG. 10. Cathodic DPVs for (a) FeZSM-5*as*, (b) FeZSM-5*c*, (c) *ex*-FeZSM-5, (d) hematite, and (e) goethite attached to GPCEs immersed into 1 M HCl; $\nu = 20\ \text{mV} \cdot \text{s}^{-1}$, $\Delta U = 80$ mV.

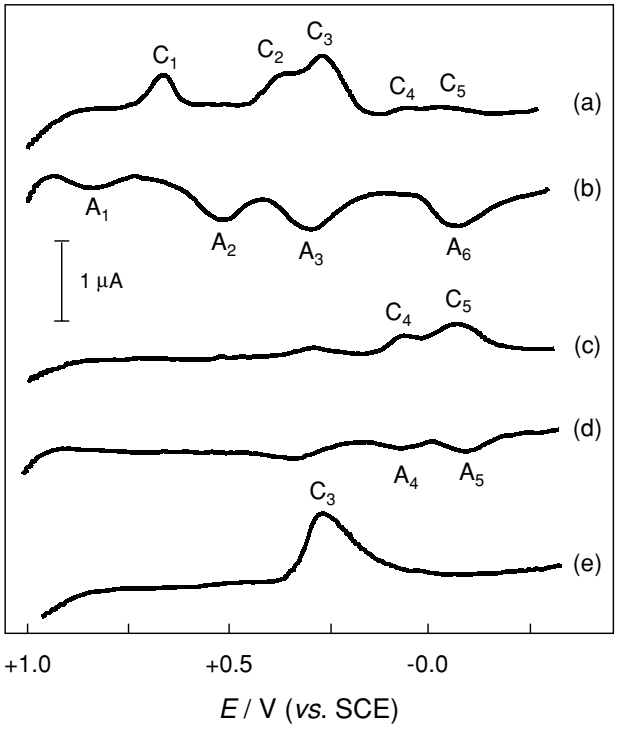

FIG. 11. Cathodic (a, c) and anodic (b, d) LSVs for GPCEs modified by (a, b) *ex*-FeZSM-5 and (c, d) FeZSM-5*as*, immersed into 0.10 M HCl. Curve (e) corresponds to the cathodic response of a 0.50 mM $FeCl_3 \cdot 6H_2O$ and 0.10 M HCl solution at an unmodified GPCE; $\nu = 20\ \text{mV} \cdot \text{s}^{-1}$.

In this manuscript, graphite–polyester composite electrodes (GPCEs) were used, which show voltammetric responses similar to the polymer film electrodes used in previous studies (52). Figure 10 shows a series of cathodic differential pulse voltammograms (DPVs) of GPCEs modified by (a) FeZSM-5*as*, (b) FeZSM-5*c*, (c) *ex*-FeZSM-5, (d) Fe_2O_3 (hematite), and (e) FeO(OH) (goethite) in 1.0 M HCl (supporting electrolyte). For FeZSM-5*as*, only peaks C_4 and C_5 are well defined. For FeZSM-5*c* and *ex*-FeZSM-5, a relatively complicated pattern can be observed, with reduction peaks at +0.65 (C_1), +0.35 (C_2), +0.28 (C_3), +0.05 (C_4), −0.15 (C_5), −0.55 (C_6), and −0.75 (C_7) V vs SCE. FeZSM-5*c* shows a voltammogram in between those of FeZSM-5*as* and *ex*-FeZSM-5. During calcination and steam treatment, peaks C_1, C_2, C_3, C_6, and C_7 develop while peaks C_4 and C_5 progressively decrease. Comparison of the voltammetric response of *ex*-FeZSM-5 with that of Fe_2O_3 and FeO(OH) clearly indicates the different electrochemical behavior of iron species in the steamed zeolite and the iron oxides.

A more detailed characterization of the electrochemical response of FeZSM-5-modified electrodes is presented in Fig. 11, in which cathodic (C) and anodic (A) linear

TABLE 4

Summary of the Electrochemical Processes Involving Iron Species in the FeZSM-5 System[a]

Peak	E_p/mV	Species involved	Assignment[b]	Electrochemical process
C_4/A_4	+50	Framework Fe ions	YE	$Z[O_3Fe^{III}(OH)]\ (b) + M^+(aq.) + e^- \rightleftharpoons Z[O_3Fe^{II}(OH)]\ (b) + M^+\ (b)$
C_5/A_5	−150			
C_1/A_1	+650	Oligonuclear oxo-Fe species	YE	$Z\text{-}Fe^{III}_xO_y(b) + x\ H^+(aq.) + x\ e^- \rightleftharpoons Z\text{-}Fe^{II}_xO_{y-x}(OH)_x\ (b)$
C_2/A_2	+300	Isolated Fe ions	YE	$Fe^{III}\text{-}Z(b) + M^+(aq.) + e^- \rightleftharpoons Fe^{II}\text{-}Z + M^+\text{-}Z\ (b)$
C_6	−550	FeO_x nanoparticles	RD	$Fe^{III}O_x + 2x\ H^+(aq.) + (2x-2)e^- \rightarrow Fe^{2+}(aq.) + x\ H_2O$
A_6	−180		OD	$Fe^{II}O_y + 2y\ H^+(aq.) \rightarrow Fe^{3+}(aq.) + y\ H_2O + (3-2y)e^-$
C_7	−750		MD	$Fe^{2+}(aq.) + 2e^- \rightarrow Fe^\circ$
C_3/A_3	+280/+360		D	$FeCl_x^{(3-x)+} + e^- \rightleftharpoons FeCl_y^{(2-y)+} + (x-y)\ Cl^-$

[a] Peak potentials (E_p) in mV vs SCE from LSVs in 0.10 M HCl electrolyte; $\nu = 20\ mV \cdot s^{-1}$. *Z*, zeolite; *b*, sites at the boundary of the zeolite; M^+, charge compensating cation.

[b] YE, electron-transfer process on iron species attached to the zeolite boundary; RD, reductive dissolution; OD, oxidative dissolution; MD, metal deposition; D, electron-transfer process involving species in solution.

scan voltammograms (LSVs) for GPCEs modified by *ex*-FeZSM-5 (a and b) and FeZSM-5*as* (c and d) immersed into 0.10 M HCl are shown. In anodic scans initiated at −0.50 V vs SCE over *ex*-FeZSM-5, peaks at −0.18 (A_6), +0.36 (A_3), +0.42 (A_2) and +0.73 (A_1) appear. Peaks A_6 and A_3 overlap the anodic counterparts of peaks C_4 and C_5, i.e., A_4 and A_5, respectively.

The electrochemical processes involved with the corresponding assignment are summarized in Table 4, based on explanations elaborated elsewhere (33, 52). The C_4/A_4 and C_5/A_5 couples, which are mainly visible in the isomorphously substituted FeZSM-5*as* sample, can be assigned to electron-transfer processes involving framework iron atoms. In this case, the peak potentials are independent of the potential scan rate and pH of the supporting electrolyte. The existence of two couples has been attributed to two different framework redox isomers having quite similar coordination environments (52). A similar situation has been recently reported by Venkatathri *et al.* (54) for vanadium-containing zeolites. The electroactive iron species can be described here in terms of $O_3Fe(OH)$ centers, similar to $O_3Ti(OH)$ redox isomers identified in titanium silicalite (55–58).

The electrode process C_6, which is characteristic of *ex*-FeZSM-5, exhibits electrochemical parameters close to those described for the reductive dissolution of iron oxides and hydrous oxides (59), which is also suggested by similarity with the electrochemical response of the reference iron oxides (especially that of hematite). The peak potential of the process C_6 shows a linear dependency with the pH of the supporting electrolyte and the potential scan, exhibiting the same behavior observed in hematite and goethite (33). The anodic process A_6 in *ex*-FeZSM-5 has been assigned to the oxidative dissolution of iron(II) nanoparticles (52). This process involves the presence of Fe(II) in the steamed sample, which is in agreement with the Fe(II) contribution identified in the Mössbauer spectrum of the fresh *ex*-FeZSM-5 sample at 300 K in air (see Fig. 8c and Table 3). The peak C_7 in *ex*-FeZSM-5 (Fig. 10c), which is also present in hematite and goethite, is attributed to the reduction of iron oxide and electrochemically generated Fe^{2+} ions to metallic iron (metal deposition in Table 4). The couple C_3/A_3 corresponds to an electron-transfer step involving Fe^{3+} ions in solution, as suggested by the presence of this couple in LSVs recorded of unmodified electrodes immersed into a diluted solution of $FeCl_3 \cdot 6H_2O$ in 0.10 M HCl (Fig. 11e). This peak is therefore attributed to a redox process involving iron-chloride complexes in solution, resulting from leaching of iron species in the zeolite boundary and reductive/oxidative dissolution processes. This is likely related to the presence of the small oxide particles.

The peak potential of the couple C_1/A_1 follows a linear dependency with the pH and the potential scan rate (not shown). In addition, the voltammetric curves exhibit a symmetric shape, which is characteristic of species strongly attached to the electrode surface. We have tentatively assigned the response to small oligonuclear oxo-iron species in the zeolite channels that remain attached to the zeolite boundary. These species undergo a rate-determining protonation process coupled with the electron-transfer step, as suggested by the slope of the E_p vs pH dependency (65 mV). The peak potential of the couple C_2/A_2 also varies linearly with the potential scan rate but it is independent of pH. This couple is attributed to a redox process involving isolated iron ions in cationic positions of the zeolite.

It can be concluded that electrochemical characterization during the different stages of the preparation of *ex*-FeZSM-5 provides unique information with respect to different iron species in the material, since different species can be identified simultaneously, based on their electrochemical activity. In the steamed catalyst, iron oxide nano-particles, iron ions in cationic positions, and oligonuclear oxo-iron species

in the zeolite channels can be distinguished. Voltammetric response techniques provide a fingerprint of the heterogeneous nature of the iron species in the catalyst. Analysis of our samples by average techniques, like EXAES, should be taken into special consideration in order to interpret the spectra properly.

CONCLUSIONS

The following physicochemical changes have been observed in the two activation steps (calcination and steam treatment) of the isomorphously substituted FeZSM-5. In the as-synthesized material complete substitution of Fe(III) ions in the zeolite framework is concluded from ^{57}Fe Mössbauer and TEM analyses. Calcination of the as-synthesized sample at 823 K leads to a complete removal of the template, but hardly affects the Al coordination. On the other hand, a considerable fraction of Fe (∼50%) is already extracted to extraframework positions. The created extraframework species are highly dispersed in the zeolite channels, mostly present as isolated or oligonuclear oxo-iron species. The presence of both Fe(III) and Fe(II) oxidation states (25% Fe(II)) after treatment in He at 623 K in FeZSM-5*c* was observed, indicating significant autoreduction of Fe(III) species. During steam treatment, hydrolysis of the Al–OH and Fe–OH bonds takes place. As a consequence, the density and strength of acid sites diminish. The extraction of Al and Fe in the steaming procedure from framework positions also leads to the formation of a broad distribution of mesopores around 11 nm. Dealumination of the zeolite framework leads to extraframework Al species with different coordination and positions in *ex*-FeZSM-5, although the nature of the Al species cannot be assessed in detail. The dislodgment of iron can be described by a clustering process, where the framework and extraframework species formed on calcination partially approach each other and accumulate as small iron oxide nanoparticles. A very homogeneous and highly dispersed distribution of these nanoparticles is obtained, with an average size of 1–2 nm. The presence of extraframework Al species plays a role in the formation of these nanoparticles and might be contained on them. A considerable fraction of the small iron oxide nanoparticles may be located inside the created mesopores, and not at the external surface of the zeolite. Other forms of iron included in the steamed catalyst consist of smaller iron species in the channels, as isolated compensating cations or oligonuclear oxo-iron species. The oxidation state of iron in the freshly steamed catalyst was assessed to be mainly Fe(III) with at least 10% Fe(II), suggesting that the steam treatment provokes the reduction of a fraction of Fe(III) species. Pretreatment of this sample in He at 623 K leads to formation of 50% Fe(II), with the difference being attributed to autoreduction of Fe(III) to Fe(II) species. The amount of the Fe(III) reduced in *ex*-FeZSM-5 depends on the extent of the He pretreatment. H_2-TPR after pretreatment of the samples with N_2O at 623 K confirms that the reduction in steamed FeZSM-5 is limited to the Fe(II) state. No reduction to metallic iron takes place.

ACKNOWLEDGMENTS

This research was financially supported by the Council for Chemical Science of the Netherlands Organization for Scientific Research (CW-NWO). G.M. and I. W.C.E.A. gratefully acknowledge a fellowship granted by the Royal Netherlands Academy of Arts and Sciences. J. C. Groen, P. J. Kooyman, and A. Sinnema are gratefully acknowledged for performing the gas adsorption, TEM, and NMR analyses, respectively.

REFERENCES

1. Venuto, P. B., *Microporous Mater.* **2**, 297 (1994).
2. Uddin, Md., Komatsu, T., and Kashima, T., *J. Catal.* **150**, 439 (1994).
3. Panov, G. I., Uriarte, A. K., Rodkin, M. A., and Sobolev, V. I., *Catal. Today* **41**, 365 (1998).
4. Dubkov, K. A., Sobolev, V. I., and Panov, G. I., *Kinet. Catal.* **39**, 72 (1998).
5. Feng, X., and Hall, W. K., *Catal. Lett.* **41**, 45 (1996).
6. Chen, H-Y., and Sachtler, W. M. H., *Catal. Today* **42**, 73 (1998).
7. Ma, A.-Z., and Grünert, W., *Chem. Commun.* 71 (1999).
8. Long, R. Q., and Yang, R. T., *J. Catal.* **188**, 332 (1999).
9. Kögel, M., Mönnig, R., Schwieger, W., Tissler, A., and Turek, T., *J. Catal.* **182**, 470 (1999).
10. Pophal, C., Yogo, T., Yamada, K., and Segawa, K., *Appl. Catal. B* **16**, 177 (1998).
11. Centi, G., and Vazanna, F., *Catal. Today* **53**, 683 (1999).
12. Mauvezin, M., Delahay, G., Kißlich, F., Coq, B., and Kieger, S., *Catal. Lett.* **62**, 41 (1999).
13. Kapteijn, F., Marbán, G., Rodríguez-Mirasol, J., and Moulijn, J. A., *J. Catal.* **167**, 256 (1997).
14. El-Malki, E. M., van Santen, R. A., and Sachtler, W. M. H., *J. Catal.* **196**, 212 (2000).
15. Long, R. Q., and Yang, R. T., *Chem. Commun.* 1651 (2000).
16. Joyner, R., and Stockenhuber, M., *J. Phys. Chem. B* **103**, 5963 (1999).
17. Rauscher, M., Kesore, K., Mönnig, R., Schwieger, W., Tißler, A., and Turek, T., *Appl. Catal. A* **184**, 249 (1999).
18. Marturano, P., Drozdová, L., Kogelbauer, A., and Prins, R., *J. Catal.* **192**, 236 (2000).
19. Battiston, A. A., Bitter, J. H., and Koningsberger, D. C., *Catal. Lett.* **66**, 75 (2000).
20. Ribera, A., Arends, I. W. C. E., de Vries, S., Pérez-Ramírez, J., and Sheldon, R. A., *J. Catal.* **195**, 287 (2000).
21. Long, R. Q., and Yang, R. T., *J. Catal.* **194**, 80 (2000).
22. El-Malki, E. M., van Santen, R. A., and Sachtler, W. M. H., *J. Phys. Chem. B* **103**, 4611 (1999).
23. Chen, H.-Y., Wang, X., and Satchler, W. M. H., *Phys. Chem. Chem. Phys.* **2**, 3083 (2000).
24. Marturano, P., Drozdová, L., Kogelbauer, A., and Prins, R., *J. Catal.* **190**, 460 (2000).
25. Battiston, A. A., Bitter, J. H., and Koningsberger, D. C., *in* "Zeolite and Mesoporous Materials at the Dawn of the 21st Century" (A. Galarneau, F. Di Renzo, F. Fajula, and J. Vedrine, Eds.), 12-O-O2, p. 133. Elsevier, Amsterdam, 2001.
26. Pérez-Ramírez, J., Kapteijn, F., Mul, G., and Moulijn, J. A., *Chem. Commun.* 693 (2001).

27. Pérez-Ramírez, J., Kapteijn, F., Mul, G., and Moulijn, J. A., *Appl. Catal. B* **35**, 227 (2001).
28. Bordiga, S., Buzzoni, R., Geobaldo, F., Lamberti, C., Giamello, E., Zecchina, A., Leofanti, G., Petrini, G., and Tozzola, G., *J. Catal*. **158**, 486 (1996).
29. Fejes, P., Nagy, J. B., Halász, J., and Oszkó, A., *Appl. Catal. A* **175**, 89 (1998).
30. Saito, A., and Foley, H. C., *Microporous Mater.* **3**, 531 (1995).
31. Barret, E. P., Joyner, L. G., and Halenda, P. H., *J. Am. Chem. Soc*. **73**, 373 (1951).
32. Lippens, B. C., and de Boer, J., *J. Catal.* **4**, 319 (1965).
33. Doménech, A., Pérez-Ramírez, J., Ribera, A., Mul, G., and Kapteijn, F., *Catal. Lett.*, in press.
34. Llewellyn, P. L., Coulomb, J.-P., Grillet, Y., Patarin, J., Lauter, H., Reichert, H., and Rouquerol, J., *Langmuir* **9**, 1846 (1993).
35. Saito, A., and Foley, H. C., *Microporous Mater.* **3**, 543 (1995).
36. Martens, J. A., Souverijns, W., Van Rhijn, W., and Jacobs, P. A., *in* "Handbook of Heterogeneous Catalysis" (G. Ertl, H. Knözinger, and J. Weitkamp, Eds.), Vol. 2, p. 336. Wiley VCH, Weinheim, 1997.
37. Gregg, S. J., and Sing, K. S. W., "Adsorption, Surface Area, and Porosity." Academic, London, 1982.
38. Llewellyn, P. L., Coulomb, J.-P., Grillet, Y., Patarin, J., Andre, G., and Rouquerol, J., *Langmuir* **9**, 1852 (1993).
39. Engelhardt, G., and Michel, D., "High-Resolution Solid-State NMR of Silicates and Zeolites." Wiley, New York, 1987.
40. Müller, M., Harvey, G., and Prins, R., *Microporous Mesoporous Mater.* **34**, 135 (2000).
41. Bodart, P. B., Nagy, J. B., Debras, G., Gabelica, Z., and Jacobs, P. A., *J. Phys. Chem.* **90**, 5183 (1986).
42. Motz, J. L., Heinichen, H., and Hölderich, W. F., *J. Mol. Catal.* **136**, 175 (1998).
43. Topsøe, N. Y., Pederson, K., and Derouane, E. G., *J. Catal.* **70**, 41 (1981).
44. Lobree, L. J., Hwang, I.-C., Reimer, J. A., and Bell, A. T., *J. Catal.* **186**, 242 (2001).
45. Lázár, K., Kotasthane, A. N., and Fejes, P., *Catal. Lett.* **57**, 171 (1999).
46. Fejes, P., Nagy, J. B., Lázár, K., and Halász, J., *Appl. Catal. A* **190**, 117 (2000).
47. Szostak, R., Nair, N., Simmons, D. K., Thomas, T. L., Kuvadia, R., Dunsion, B., and Shieh, D. C., *in* "Innovations in Zeolite Materials Science" (P. J. Grobet, *et al.,* Eds.), p. 403. Elsevier, Amsterdam, (1988).
48. Meagher, A., Nair, V., and Szostak, R., *Zeolites* **8**, 3 (1988).
49. Yuen, S., Chen, Y., Kubsh, J. E., Dumesic, J. A., Topsøe, N., and Topsøe, H., *J. Phys. Chem.* **86**, 3022 (1982).
50. Calis, G., Frenken, P., de Boer, E., Swolfs, A., and Hefni, M. A., *Zeolites* **7**, 319 (1987).
51. Ovanesyan, N. S., Dubkov, K. A., Pyalling, A. A., and Shteinman, A. A., *J. Radioanal. Nucl. Chem.* **246**, 149 (2000).
52. Doménech, A., Pérez-Ramírez, J., Ribera, A., Mul, G., Kapteijn, F., and Arends, I. W. C. E., *J. Electroanal. Chem.* **519**, 72 (2002).
53. Bessel, C. A., and Rolison, D. R., *J. Phys. Chem. B* **101**, 1148 (1997).
54. Venkatathri, N., Vinod, M. P., Vijayamohanan, K., and Sivasanker, S., *J. Chem. Soc., Faraday Trans*. **92**, 473 (1996).
55. Geobaldo, F., Bordiga, S., Zecchina, A., Gianello, E., Leofanti, G., and Petrini, G., *Catal. Lett.* **16**, 109 (1992).
56. Arbuznikov, A. V., and Zhidomirov, G. M., *Catal. Lett*. **40**, 17 (1996).
57. Rodrigues, S., Munichandraiah, N., and Shukla, A. K., *J. Appl. Electrochem.* **28**, 1235 (1998).
58. de Castro Martins, S., Tuel, A., and Ben Taârit, Y., *Stud. Surf. Sci. Catal*. **84**, 501 (1994).
59. Grygar, T., *J. Electroanal. Chem*. **405**, 117 (1996).